Journal of Alloys and Compounds 773 (2019) 605–611

Contents lists available at ScienceDirect

Journal of Alloys and Compounds

journal homepage: http://www.elsevier.com/locate/jalcom

Temperature effects on magnetic properties of Fe_3O_4 nanoparticles synthesized by the sol-gel explosion-assisted method

Ping Hu [a, b, *], Tian Chang [a, b], Wen-Jing Chen [a, b], Jie Deng [a, b], Shi-Lei Li [a, b], Ye-Gai Zuo [a], Lu Kang [a], Fan Yang [a, b], Megan Hostetter [c], Alex A. Volinsky [c]

[a] School of Metallurgy Engineering, Xi'an University of Architecture and Technology, Xi'an, 710055, China
[b] State Local Joint Engineering Research Center for Functional Materials Processing, Xi'an, 710055, China
[c] Department of Mechanical Engineering, University of South Florida, Tampa, FL, 33620, USA

ARTICLE INFO

Article history:
Received 4 August 2018
Received in revised form
17 September 2018
Accepted 18 September 2018
Available online 19 September 2018

Keywords:
Sol-gel explosion-assisted
Monodispersed
Verwey transition
Magnetic behavior

ABSTRACT

Fe_3O_4 nanoparticles were successfully synthesized by the sol-gel explosion-assisted method. The phase composition of products with different ratios of dry gel and explosive agent (3:1, 6:1, 12:1) was studied. Highly pure, well-crystallized, spherical and monodispersed Fe_3O_4 3–20 nm nanoparticles were obtained at the 12:1 ratio. X-ray photoelectron spectroscopy characterization of the as-synthesized nanoparticles demonstrated consistency with stoichiometric Fe_3O_4 surface composition. Zero-field cooled and field cooled measurements at 200 Oe validate that the anisotropy energy is greater than thermal energy up to 300 K for the ~10 nm samples. The Verwey transition (metal-insulator) of magnetite nanoparticles takes place at 128 K (T_v). The effects of different temperatures of 5 K, 128 K, and 300 K on magnetic behavior were studied in detail. The results show that hysteresis behavior weakens as the temperature increases. Saturation magnetization (M_s) of 86.2 emu/g is the highest at T_v. Initial susceptibility (χ_α) increases as a function of temperature, whereas coercivity (H_c) decreases.

1. Introduction

Nano-sized magnetic materials have been immensely researched because of their different and improved functionality compared to their bulk counterparts. Fe_3O_4 is among the most widely studied metal oxide nanoparticle systems and has gained more scientific and technological attention due to its wide range of applications in magnetic resonance imaging [1], drug delivery [2], environmental remediation [3,4] and heterogeneous catalysis [5]. It also attracts academic interest because of the special Verwey transition, which is a metal to insulator transition with a sharp change in conductivity, heat capacity, coercivity and magnetization [6]. Fe_3O_4 belongs to the inverse spinel family with the $[Fe^{3+}]_{Tetra}[Fe^{2+}Fe^{3+}]_{Octra}O_4$ chemical formula. The material is conductive and ferromagnetic with a high Curie temperature of $T_c = 850$ K, with nearly full spin polarization at room temperature [7].

Recently, several methods have been used to prepare Fe_3O_4 nanostructures, including hydrothermal [8], co-precipitation [9], sol-gel [10], thermal decomposition [11] and micro-emulsion [12] methods. However, all the above synthesis methods often require long production cycle, complicated operating steps, and poor reproducibility, which rendered them unsuitable for large-scale production.

In this study, based on the nano-powder synthesis technology of diamond and graphite [13], we introduced a weak explosive agent (picric acid) into the synthesis of Fe_3O_4 nanoparticles, and developed a sol-gel explosion-assisted method for rapid synthesis of small particles with good dispersibility of Fe_3O_4 nanoparticles. This method has high yield in the sol-gel process; and the action of the explosion field prevents magnetic nanoparticles tendency to easily agglomerate.

The phase composition of products with different ratios of dry gel and explosive agent (3:1, 6:1, 12:1) was analyzed. The microstructure along with the synthesis mechanism was also studied. The metal-insulator transition (the Verwey transition) temperature (T_v) of Fe_3O_4 was confirmed in this work. The effects of different temperatures ($T < T_v$, T_v, and $T > T_v$) on magnetic behavior have been thoroughly studied.

---

* Corresponding author. School of Metallurgy Engineering, Xi'an University of Architecture and Technology, Xi'an, 710055, China.
E-mail address: huping1985@126.com (P. Hu).

https://doi.org/10.1016/j.jallcom.2018.09.238

2. Experimental

2.1. Synthesis of Fe_3O_4 nanoparticles

Ferric nitrate and citric acid with a molar ratio of 1:0.8 were dissolved in 113 ml of deionized water, and the material was fully dissolved by electromagnetic stirring at 35 °C for 30 min. Ammonia was added dropwise to adjust the solution pH to 7.3. Then the reaction was carried out at 68 °C for 4 h. Afterwards, the solution was evaporated to a viscous state at 95 °C. When a sol-like substance was formed, it was quickly poured onto a tray. The dry gel particles and picric acid were homogeneously mixed in the autoclave filled with Ar. The autoclave was moved to a heating furnace and kept at 450 °C for a while, and finally loose black powder products were obtained after water cooling to room temperature. The products were washed with ethanol in an ultrasonic cleaner three times, and separated with a magnet. The products prepared in this work were named Y_i-X_i, where Y_i ($i = 1, 2, 3$) represent the mass ratio of dry gel and picric acid, corresponding to 3:1, 6:1, and 12:1, respectively. X_i ($i = 1, 2, 3$) means holding time, which is 60, 40, and 20 min, respectively.

2.2. Materials characterization

The phase composition of the Fe_3O_4 nanoparticles was analyzed using X-ray diffractometer (XRD, D8, Buber, Germany, Cu Kα radiation, $\lambda = 0.15414$ nm). The element states were investigated by the X-ray photoelectron spectroscopy (XPS, PHI Quantera SXM) with the Al-Kα excitation source. The morphology and size of particles were observed by transmission electron microscope (TEM, JEM-2100 Plus, Japan) operated at 200 kV. The intrinsic magnetic properties of the samples were measured with a vibrating sample magnetometer (VSM, MPMS-SQUID VSM-094, USA).

3. Results and discussion

3.1. Structure characterization

XRD patterns of products with different picric acid ratios and holding times are shown in Fig. 1. At $Y_1 = 3:1$, FeO and $FeCO_3$ appeared in addition to the $Fe_3O_4^*$ phase. Spinel iron oxide (Fe_3O_4 and Fe_2O_3) cannot be distinguished by XRD results alone, so it is assumed here as $Fe_3O_4^*$. Moreover, the relative intensity of the diffraction peaks of FeO decreased with shorter holding time, which means that longer holding time and higher picric acid ratio lead to over-reduction of the product.

Therefore, the heat treatment at different holding times was also performed at $Y = 6:1$ and 12:1. It can be seen from Fig. 1(b) that compared with the ratio of 3:1, the number of FeO diffraction peaks at the 6:1 ratio is significantly reduced and the relative intensity is weakened. When the ratio was reduced to 12:1, $Fe_3O_4^*$ phase was successfully synthesized. Fig. 1 (c) shows that the diffraction peaks of the Y_3-X_1 samples are consistent with the $Fe_3O_4^*$ standard peak. Strong and sharp diffraction peaks indicate that the $Fe_3O_4^*$ is well crystallized.

X-ray photoelectron spectroscopy (XPS) is a versatile surface analysis technique that can be used for compositional and chemical states analysis. It has been shown in previous studies that the peak positions of Fe $2p_{1/2}$ and Fe $2p_{3/2}$ depend on the ionic states of Fe [14–17]. The positions of the satellite Fe $2p_{1/2}$ and Fe $2p_{3/2}$ peaks are also very sensitive to the oxidation states and these peaks have been used to qualitatively determine the ionic states of iron. It has been previously reported that Fe $2p_{3/2}$ in Fe_3O_4 does not have a satellite peak [18]. The absence of the satellite peak has been also confirmed in this study in Fig. 2(a). The peak positions of Fe $2p_{1/2}$ and Fe $2p_{3/2}$ are 710.2 and 724 eV, respectively. They are located between the values for the $2FeO \cdot SiO_2$ and Fe_2O_3 standard samples [18].

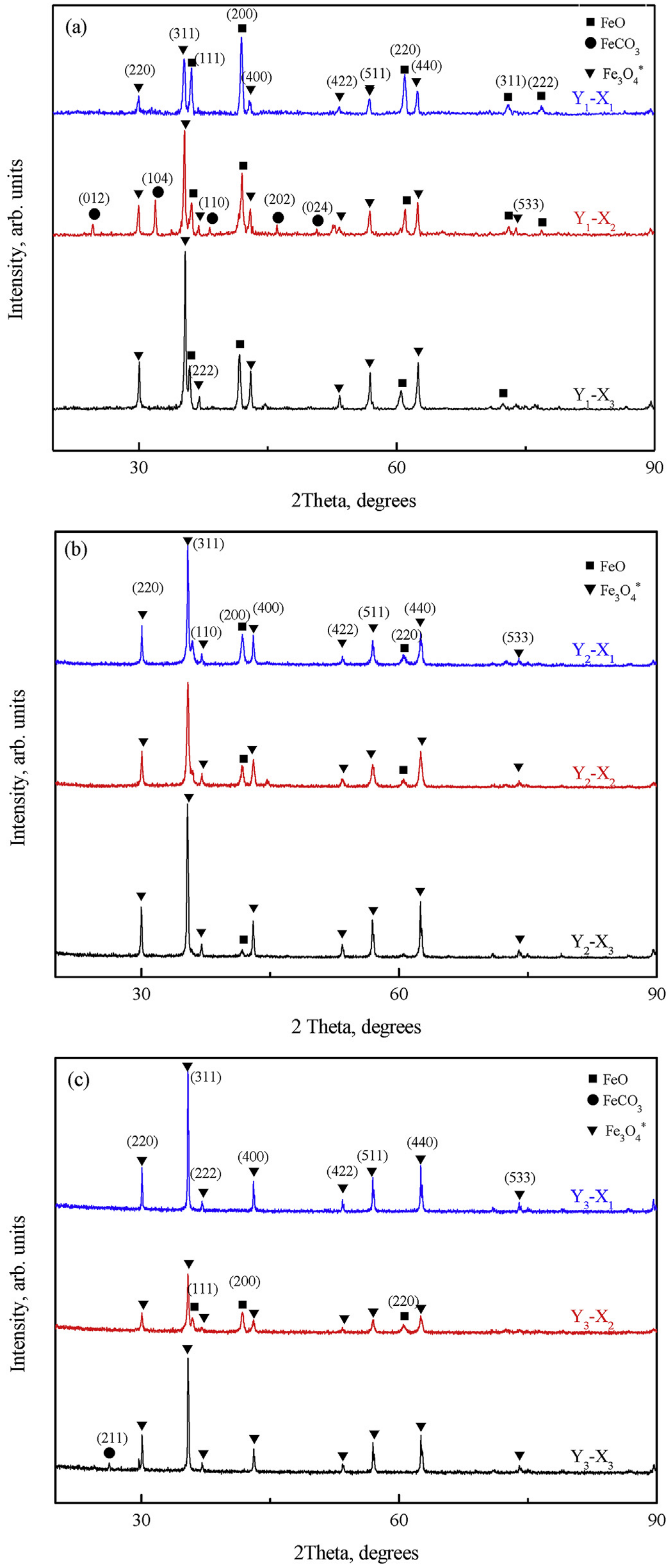

Fig. 1. XRD patterns of products with different picric acid ratios and holding time: (a) 3:1 and 60, 40, and 20 min, (b) 6:1, (c) 12:1.

The 2p peaks are separated into two peaks. To obtain the total

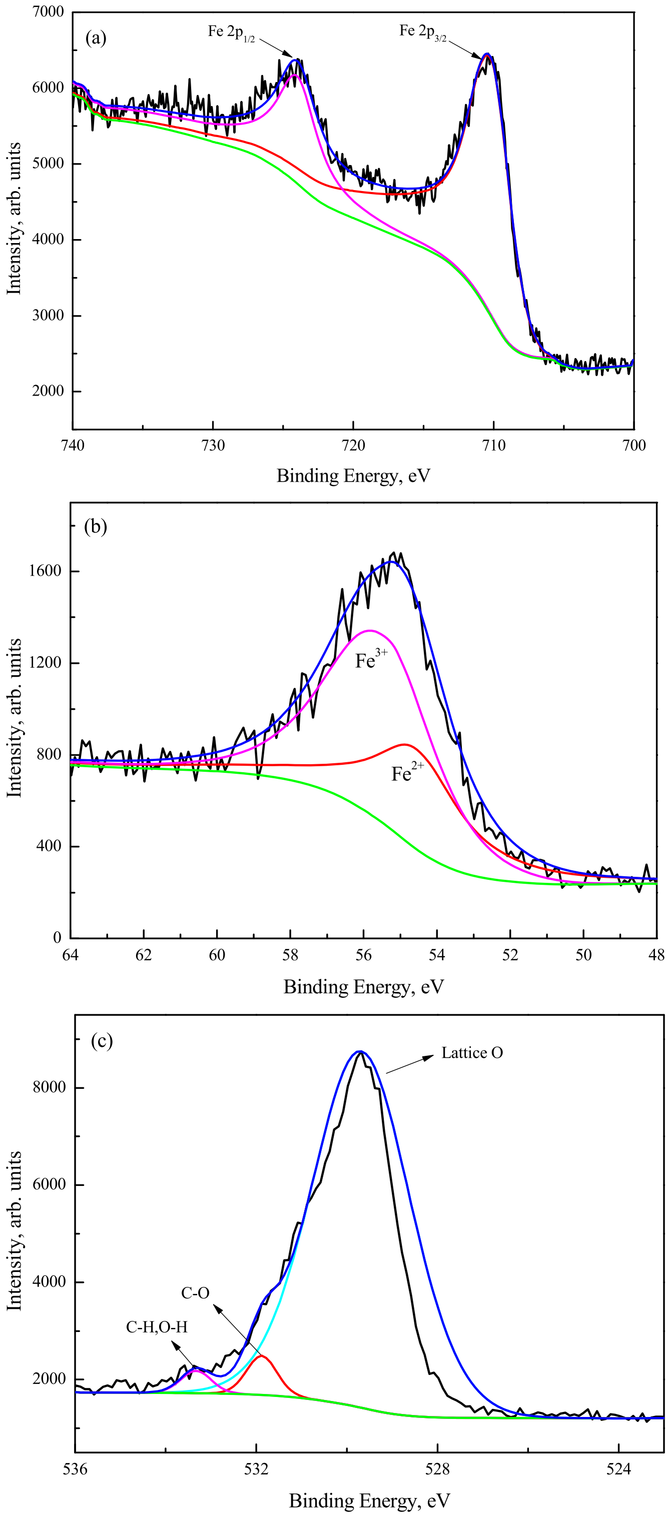

Fig. 2. XPS spectra for the as-synthesized Y_3-X_1 sample: (a) Fe 2p, (b) Fe 3p, (c) O 1s.

contribution, the intensities of both contributions have to be integrated. The base intensities of Fe $2p_{1/2}$ and Fe $2p_{3/2}$ are significantly different and appear to vary in a non-linear way with binding energy. Therefore, it is not possible to accurately subtract the background signal.

The Fe 3p peak is a single peak without any interfering satellite peaks. Fe 3p peaks are used in the present study for the quantitative analysis of Fe^{3+} and Fe^{2+} [18]. Using the peak shape parameters and peak positions of Fe^{2+} and Fe^{3+} obtained from the previous study of $2FeO\cdot SiO_2$ and Fe_2O_3, the Fe 3p peak for Fe_3O_4 was deconvoluted into the Fe^{2+} and Fe^{3+} peaks in Fig. 2(b). It shows that the Fe 3p peak position for Fe^{2+} is 54.5 eV and for Fe^{3+} it is 55.4 eV. The peak width (FWHM) of the Fe 3p peak for Fe^{3+} (3.49 eV) is larger than Fe^{2+} (2.96 eV).

The FWHM, ΔE, is described as follows [17].

$$\Delta E = \left(\Delta E_{n}^{2} + \Delta E_{P}^{2} + \Delta E_{a}^{2}\right)^{1/2} \qquad (1)$$

Here, ΔE_n is the inherent width of the core level, ΔE_p is the width of the X-ray line and ΔE_a is the analyzer resolution. Since all the data were taken under the same conditions, ΔE_p and are considered constant for all peaks. The inherent line width of a core level is a direct reflection of the lifetime of the ion state remaining after photoemission. The line width is inversely proportional to the lifetime of the ion state remaining after photoemission [17]. The electronic configuration of Fe^{3+} is $3d^5$, while that of Fe^{2+} is $3d^6$. This means that Fe^{2+} will have a longer lifetime than Fe^{3+}. Therefore, the FWHM of the Fe^{2+} peak is expected to be smaller than of the Fe^{3+} peak.

Stoichiometric Fe_3O_4 can also be expressed as $FeO\cdot Fe_2O_3$, thus the Fe^{2+}:Fe^{3+} ratio should be 1:2. The results of the deconvoluted peaks using the parameters defined above give Fe^{2+}:Fe^{3+} = 1.07:2. This value is close to the stoichiometric ratio of Fe^{2+} and Fe^{3+} for Fe_3O_4. It indicates that the prepared spinel iron oxide is pure Fe_3O_4 instead of Fe_2O_3.

Fig. 2(c) shows the lattice O 1s XPS spectrum for the Y_3-X_1 sample. The spectrum can be fitted with three peaks with binding energy of 529.7, 531.9 and 533.3 eV. The most intense peak at 529.7 eV results from lattice oxygen in Fe_3O_4. The peak at 531.9 eV is due to the C—O bond. The third peak at 533.3 eV corresponds to a combination of the C—H and O—H bonds. These two peaks are attributed to the organic acid used in the experiment.

3.2. *Micromorphology characterization*

Fig. 3 (a) shows the TEM micrographs of the Y_3-X_1 sample, in which mono-dispersed and spherical particles were observed with a narrow size distribution of 3—20 nm. The selected area electron diffraction (SAED) pattern depicts their polycrystalline nature (inset image). The high resolution TEM image in Fig. 3(b) shows the clear and continuous lattice fringes of Fe_3O_4, suggesting that the Fe_3O_4 nanoparticles have good crystalline structure. The distance between neighbouring lattice fringes was measured to be 0.485 nm, which is close to the (111) lattice spacing of Fe_3O_4.

4. Synthesis mechanism

4.1. *The complexation of citric acid and metal ions*

The sol-gel explosion-assisted method for the preparation of Fe_3O_4 nanoparticles uses iron nitrate as an iron source and citric acid as a chelating agent. As shown in Fig. 4, the OH^- ions in the system lose water with the H^+ ionized by the carboxylic acid group in citric acid. The carboxylic acid group has a stabilizing effect on NH_4^+, then causing the electron pair to provide an N atom, which forms a complex with metal ions. Therefore, for the citric acid structure, the carboxylic acid group is the most influential after complexation. The possible molecular structure of the iron-containing complexes formed after the sol-gel shows a network-like space structure shown in Fig. 4.

Citric acid not only serves as an organic carbon source, a

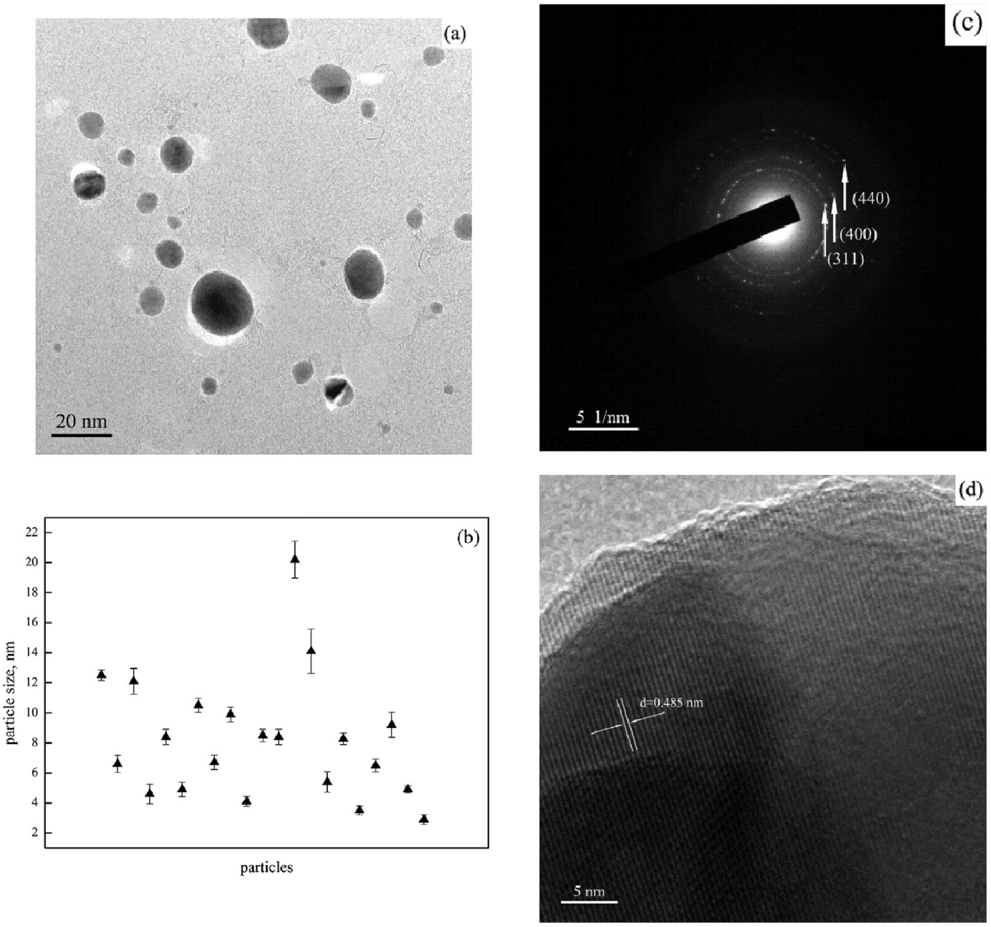

Fig. 3. (a) TEM image, (b) particle size distribution diagram, (c) SAED pattern, (d) lattice fringes of Y_3-X_1.

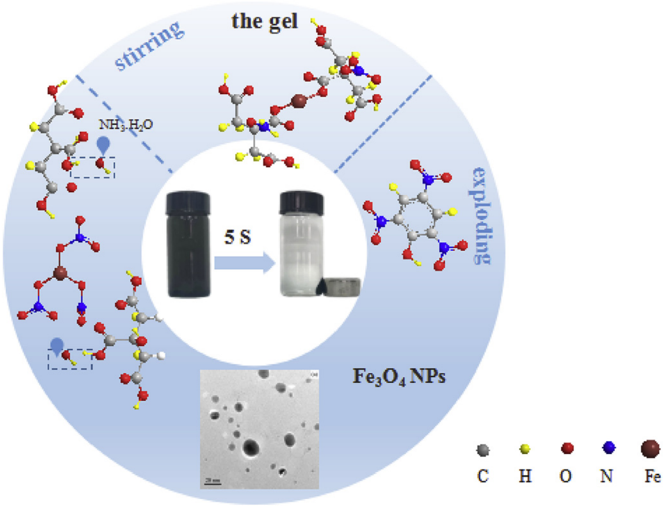

Fig. 4. Synthesis mechanism of the Fe_3O_4 nanoparticles via the sol-gel explosion-assisted method.

stoichiometric overdose of citric acid also cracks out highly active carbon atoms during the explosion process, allowing dry gel to undergo combustion decomposition and carbothermal reduction reaction simultaneously.

4.2. Explosion action mechanism

A weak explosive picric acid was added in the carbothermal reduction process of dry gel. The explosion point is around 300 °C. Its explosive reaction follows Eq. (2). Picric acid will be completely decomposed under the experimental conditions, and will not limit the subsequent application of the product.

$$2C_6H_3N_3O_7 \rightarrow 3H_2O(g)\uparrow + 3N_2\uparrow + 11CO\uparrow + C \qquad (2)$$

The gas generated by the explosion, high temperature and pressure provide basic materials and energy for the synthesis and phase transformation of nanoparticles. The gaseous-like free carbon produced by the negative-oxygen-balanced explosive during the explosion is deposited on the surface of the nanoparticles, exerting a steric hindrance effect and preventing the growth and agglomeration of the nanoparticles.

5. Magnetic properties temperature dependence

To better understand the magnetic properties of magnetite nanoparticles, we performed magnetization measurements as a function of temperature. The magnetization behavior of the sample as a function of temperature was measured under the zero-field cooled (ZFC) and field cooled (FC) conditions with an applied magnetic field of 200 Oe, as shown in Fig. 5. These nanoparticles show a clear prominent ZFC curve at 128 K, depicting the metal-insulator transition (the Verwey transition) temperature T_v of

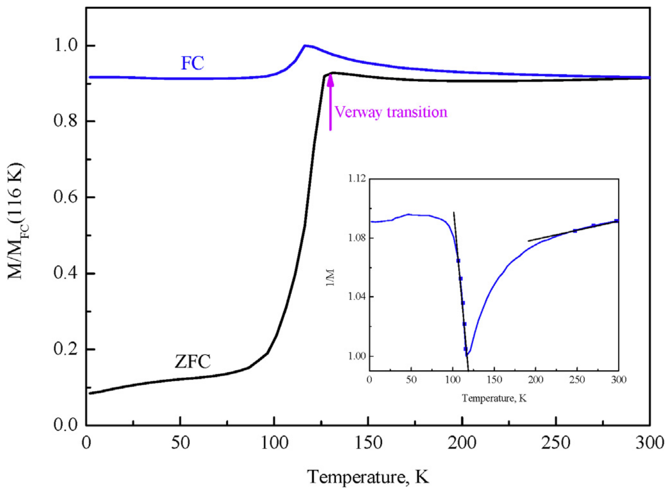

Fig. 5. The measured and simulated zero field cooled and field cooled magnetization curves in the 200 Oe field. The magnetization is normalized to M_{FC} (116 K). The insets show the reciprocal of the normalized M_{FC} vs T.

Fe_3O_4 [19–21].

The origin of this transition remains to be solved [6]. The most believed scenario has been the charge ordering. The electron carriers localized at low temperatures, forming a periodic arrangement in some narrow band strongly correlated electron systems, i.e. a charge-ordered state. Below T_v, the Fe^{3+} and Fe^{2+} ions will show a periodic and orderly arrangement on the grid, and Fe_3O_4 assumes a charge-ordered insulating state. As a result, the resistivity and distortion of the cubic symmetry increased. However, above the T_v they become statistically distributed over the B-sublattice (with the possible preservation of the short-range order), thus exhibiting metallic states.

The FC curve represents the thermal equilibrium states of the sample. Therefore, the curve is described by the Curie-Weiss law [22]:

$$\chi = \frac{M}{H} = \frac{C}{(T-\theta)} \tag{3}$$

Here, χ is susceptibility, C is Curie constant and θ is Weiss constant.

To observe the interactions between particles in the aggregates, the inverse of the magnetization at low fields was plotted versus temperature. The linear behavior was extrapolated to find out whether it goes to zero, positive, or negative values of T. That is the positive and negative of the θ value. In the case of non-interacting magnetic nanoparticles, the extrapolation should go to zero [23].

In the present case, by fitting the data to the Curie-Weiss law, we find that the extrapolation of the linear regime gives a positive value of θ in the 100–128 K range, indicating the ferromagnetic-like character of the interactions of the nanoparticles inside the aggregates. However, the antiferromagnetic-like character of the interaction is shown in the 200–300 K range as a result of the negative value.

ZFC-FC measurements at 200 Oe field do not show blocking temperature for synthesized sample, confirming that the anisotropy energy is greater than the thermal energy up to 300 K [24]. Skumryev et al. have recently shown that it is possible to beat the superparamagnetic limit by the formation of exchange bias interactions [25] caused by several factors, including magnetic coupling at the interface and uncompensated spins on the surface. In addition, the superparamagnetic relaxation time is usually described by the Arrhenius's law [26] when the interaction between particles is negligible.

$$\tau = \tau_0 e^{KV/K_BT} \tag{4}$$

Here, τ is preexponential factor of relaxation time, τ_0 is preexponential factor of characteristic relaxation time, K is the magnetocrystalline anisotropy constant, V is the volume of the particles and K_B is Boltzmann constant. The smaller the particle size and the higher the temperature, the easier it is to observe superparamagnetism. Superparamagnetism is not only related to particle size and temperature, but also closely related to the characteristic measurement time of the instrument. If the measured characteristic time is longer than the relaxation time of the particle magnetic moment, when the mean value of the magnetic moment is zero, and the sample will exhibit superparamagnetism.

As shown in Fig. 6, the initial magnetization curve at different temperatures can be divided into five characteristic stages. Region 1 is the initial or reversible region under weak magnetic field. At this time, M = χ_α H, χ_α is the characteristic constant of ferromagnetism, which is called initial susceptibility. The χ_α at 5 K, 128 K, and 300 K is 0.023, 0.033, and 0.041, respectively. It can be seen that χ_α increases with the test temperature. Magnetization increases sharply, and the magnetic susceptibility passes through its maximum value χ_m in region 3 of a medium intensity magnetic field. The χ_m at 5 K is the smallest. The Barkhausen jumps appear in this area, signifying the violent magnetization process [27]. The domain wall exhibits multiple jump displacements, namely Barkhausen jumps, which is a feature of irreversible magnetization, and irreversible magnetization leads to hysteresis. Magnetization curve slowly rises, and finally tends to a horizontal saturation line in region 4. The magnetization saturation (M_s) at 128 K is the largest and the Ms at 300 K is the smallest. In region 5, the paramagnetic region appears under stronger magnetic field. Only under a sufficiently strong magnetic field can there be a paramagnetic magnetization process.

When the external magnetic field H is applied, the ferromagnet begins to be magnetized, and a non-zero magnetization δI_H appears along the direction of H, where v_i is the volume of the ith magnetic domain, θ_i is the angle between the magnetic vector I_S of the i domain and any particular direction.

$$\delta I_H = \sum_i (I_S \cos\theta_i \delta v_i - I_S v_i \sin\theta_i \delta\theta_i + v_i \cos\theta_i \delta I_s) \tag{5}$$

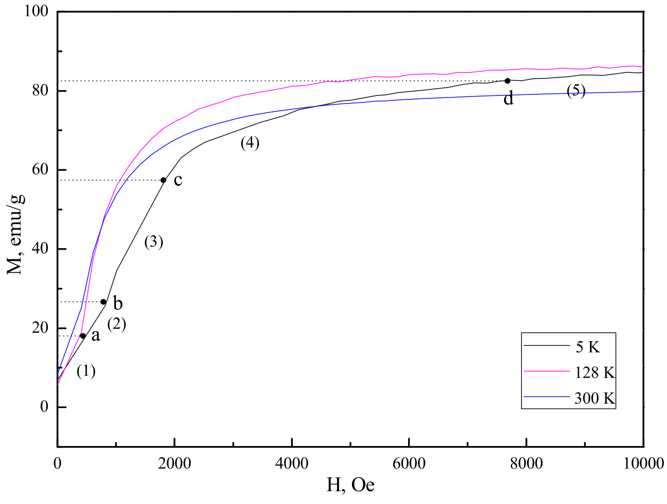

Fig. 6. Initial magnetization curves of the Y_3-X_1 nanoparticles at different temperatures.

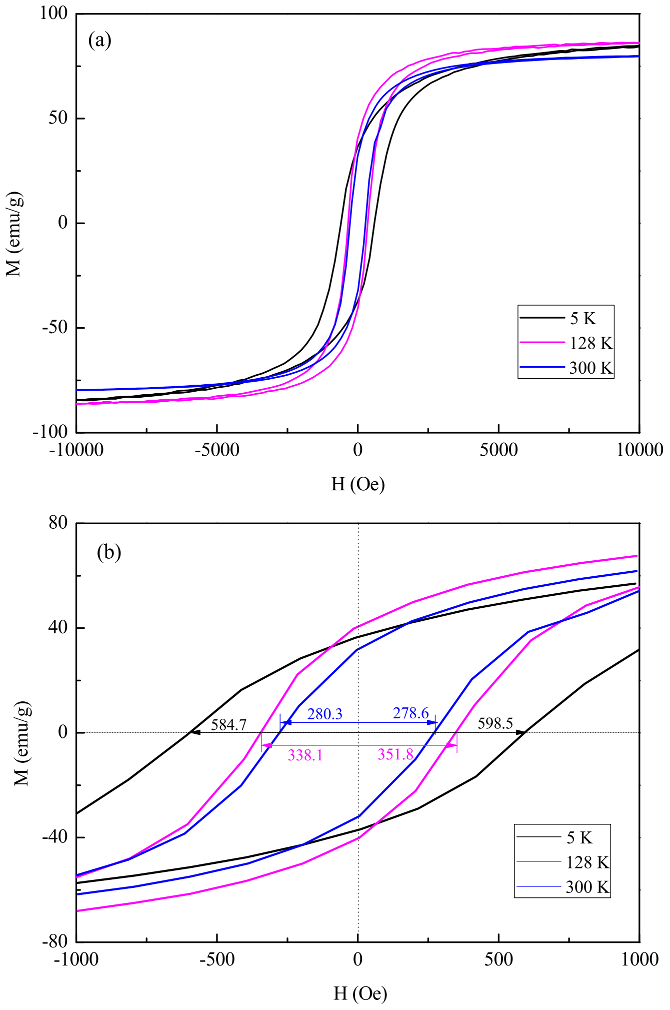

Fig. 7. (a) The hysteresis loops of the as-synthesized Fe_3O_4 nanoparticles at different temperatures, (b) Magnified diagram at the origin of hysteresis loops.

The first term represents the contribution of magnetic domain growth to the total magnetization near the direction of the external magnetic field. This process is performed by the displacement of the wall of the magnetic domain, which is referred to as the domain wall displacement process. The second term represents the contribution of the direction of the magnetization vector I_S to the total magnetization, referred to as the magnetic domain rotation process. The third term represents an increase in the number of positive spin magnetic moments in the unit volume, which is referred to as the paramagnetic process.

Generally, the domain wall displacement plays a major role in the weak magnetic field (1, 2 and 3 regions). Conversely, the magnetic domain rotation plays a major role in the strong magnetic field. That is, the energy required for rotation is higher. Both types of magnetization can be either reversible or irreversible, and the irreversible process causes all hysteresis.

The hysteresis loops of Fe_3O_4 nanoparticles at different temperatures are shown in Fig. 7(a). The M_s values at 5 K, 128 K and 300 K are 84.6 emu/g, 86.2 emu/g and 79.7 emu/g, respectively. Obviously, the M_s is the highest at 128 K. The reported value of saturation magnetization in their bulk counterpart is 92 emu/g [28]. The lower value of magnetization can be either due to the finite size effect and change in cation distribution, shape effect or any other reasons like spin pinning, spin canting, crystal defects, etc. This is because of the increasing surface to volume ratio of the particle with smaller size. The spin moment present on the particle surface have random alignment as the number of neighbouring atoms surrounded the spin are less compared to the spin moment of core atoms.

Magnetic hysteresis behavior weakens with the temperature increase. From Fig. 7(b), it is observed that H_c decreases with temperature. The coercivity of the Fe_3O_4 NPs is larger than that of the bulk materials (<10 Oe) [29], which also occurs in the preparation of ferrite nanoparticles. This is due to spin barriers, spin tilt and spin glass effects induced by in situ chemical disordering on the surface of nanoparticles [30]. Moreover, the surface atoms of the nanoparticles deviate from the normal positions, resulting in lattice distortion, which increases the surface barrier of the nanoparticles. In addition, it is found that the hysteresis loops are asymmetrical, mainly with respect to the translation of the transverse axis. Following Néel, the magnetic energy barrier can be defined from the following relationship: $H_c = 2K/M_s$ [24]. The calculated values of K at different temperature are listed in Table 1. It is seen that the anisotropy constant K obviously decreases with increasing temperature.

As shown in Fig. 7 (a), the Fe_3O_4 nanoparticles can be easily separated from solutions using a permanent magnet within 5 s, indicating that it has a high magnetic response sensitivity. Based on the advantage of easy magnetic separation, it can be used as a magnetic adsorber to treat heavy metal ions, colored dyes, and other pollutants in wastewater. Because of the non-toxic characteristics, good biocompatibility, simple preparation, strong adsorption capacity and recycling capability, it has very broad application prospects in the restoration of water environment.

6. Conclusions

Monodisperse Fe_3O_4 nanoparticles with 3–20 nm size were successfully synthesized by an explosion-assisted sol-gel method. The synthesis mechanism is a joint action of complexation of citric acid with metal ions and the explosive field. A series of experiments were carried out under different ratios of dry gel and explosive agent (3:1, 6:1, 12:1). The peak positions of Fe $2p_{1/2}$ and Fe $2p_{3/2}$ are 710.2 and 724 eV, respectively. XPS Fe 3p peak is used in this work for the quantitative analysis of Fe^{3+} and Fe^{2+}. The results of the deconvoluted peaks give Fe^{2+}:Fe^{3+} = 1.07:2, and this value is close to the stoichiometric ratio of Fe^{2+} and Fe^{3+} for Fe_3O_4. The highly pure, well-crystallized Fe_3O_4 nanoparticles were confirmed by XRD and XPS. Zero-field cooled (ZFC) and field cooled (FC) measurements at 200 Oe validate that the anisotropy energy is greater than

Table 1
Magnetic parameters of the as-synthesized Fe3O4 nanoparticles under different temperatures.

T (K)	χ_α	M_s emu/g	M_r emu/g	Squareness ratio M_r/M_s	H_c, Oe		$K = M_s \cdot H_c/2$	
					H_c (−)	H_c (+)	K (−)	K (+)
5	0.023	84.6	36.6	0.43	584.7	598.5	24732.8	25316.6
128	0.033	86.2	40.8	0.47	338.1	351.8	14572.1	15162.6
300	0.041	79.7	31.7	0.39	280.3	278.6	11170	11102.2

thermal energy up to 300 K for ~10 nm samples. These nanoparticles show a clear prominent in the ZFC curve at 128 K, that is, the metal-insulator transition (the Verwey transition) temperature T_v of Fe_3O_4. The effects of different temperatures of 5 K, 128 K, and 300 K on magnetic behavior were studied in detail. The results show that hysteresis behavior weakens as the temperature increases. Saturation magnetization (M_s) of 86.2emu/g is the highest at T_v. Initial susceptibility (χ_α) increases with temperature, whereas coercivity (H_c) decreases. As-synthesized high magnetic response sensitivity Fe_3O_4 nanoparticles can be used as a magnetic adsorbent to treat heavy metal ions, colored dyes, and other pollutants in wastewater due to its advantage of easy magnetic separation.

Acknowledgments

This work was supported by the National Natural Science Foundation of China (NSFC, 51404181), the Youth Science and Technology New Star Project of the Shaanxi Province Innovation Ability Support Plan (2017KJXX-63), the International scientific and technological cooperation program of Shaanxi Province Innovation Ability Support Plan (2018KW-053), the Postdoctoral Science Foundation of Shaanxi Province (2017).

References

[1] L. Wang, K.G. Neoh, E.T. Kang, B. Shuter, S.C. Wang, Superparamagnetic hyperbranched polyglycerol-grafted Fe_3O_4 nanoparticles as a novel magnetic resonance imaging contrast agent: an in vitro assessment, Adv. Funct. Mater. 19 (16) (2010) 2615–2622.

[2] M.I. Majeed, Q. Lu, W. Yan, Z. Li, I. Hussain, M.N. Tahir, W. Tremele, B. Tan, Highly water-soluble magnetic iron oxide (Fe_3O_4) nanoparticles for drug delivery: enhanced in vitro therapeutic efficacy of doxorubicin and MION conjugates, J. Mater. Chem. B 1 (22) (2013) 2874–2884.

[3] X. Zhang, M. Lin, X. Lin, C. Zhang, H. Wei, H. Zhang, Polypyrrole-enveloped Pd and Fe_3O_4 nanoparticle binary hollow and bowl-like superstructures as recyclable catalysts for industrial wastewater treatment, ACS Appl. Mater. Interfaces 6 (1) (2014) 450–458.

[4] J.F. Liu, Z.S. Zhao, G.B. Jiang, Coating Fe_3O_4 magnetic nanoparticles with humic acid for high efficient removal of heavy metals in water, Environ. Sci. Technol. 42 (18) (2015) 6949–6954.

[5] M.M. Moghaddam, B. Pieber, T. Glasnov, C.O. Kappe, Immobilized iron oxide nanoparticles as stable and reusable catalysts for hydrazine-mediated nitro reductions in continuous flow, Chemsuschem 7 (11) (2014) 3122–3131.

[6] F. Walz, The Verwey transition - a topical review, J. Phys. Condens. Matter 14 (12) (2002).

[7] G.F. Goya, T.S. Berquó, F.C. Fonseca, M.P. Morale, Static and dynamic magnetic properties of spherical magnetite nanoparticles, J. Appl. Phys. 94 (5) (2003) 3520–3528.

[8] H. Zhang, G. Zhu, One-step hydrothermal synthesis of magnetic Fe_3O_4 nanoparticles immobilized on polyamide fabric, Appl. Surf. Sci. 258 (11) (2012) 4952–4959.

[9] S. Wu, A. Sun, F. Zhai, J. Wang, W. Xu, Q. Zhang, A.A. Volinsky, Fe_3O_4, magnetic nanoparticles synthesis from tailings by ultrasonic chemical co-precipitation, Mater. Lett. 65 (12) (2011) 1882–1884.

[10] N.J. Tang, W. Zhong, H.Y. Jiang, X.L. Wu, W. Liu, Y.W. Du, Nanostructured magnetite (Fe_3O_4) thin films prepared by sol–gel method, J. Magn. Magn Mater. 282 (1) (2004) 92–95.

[11] Y. Eom, M. Abbas, H.Y. Noh, C.G. Kim, Morphology-controlled synthesis of highly crystalline Fe_3O_4 and $CoFe_2O_4$ nanoparticles using a facile thermal decomposition method, RSC Adv. 6 (19) (2016) 15861–15867.

[12] Y. Li, R. Jiang, T. Liu, H. Lv, L. Zhou, X. Zhang, One-pot synthesis of grass-like Fe_3O_4, nanostructures by a novel microemulsion-assisted solvothermal method, Ceram. Int. 40 (1) (2014) 1059–1063.

[13] C. Wen, Z. Jin, X. Liu, D. Sun, X. Li, G. Zhou, J. Lin, Z. Hao, Synthesis of diamond using nano-graphite and Fe powder under high pressure and high temperature, Mater. Lett. 60 (29) (2006) 3507–3510.

[14] S.J. Roosendaal, B.V. Asselen, J.W. Elsenaar, A.M. Vredenberg, F.H.P.M. Habraken, The oxidation state of Fe(100) after initial oxidation in O_2, Surf. Sci. 442 (3) (1999) 329–337.

[15] C. Ruby, B. Humbert, J. Fusy, Surface and interface properties of epitaxial iron oxide thin films deposited on MgO(001) studied by XPS and Raman spectroscopy, Surf. Interface Anal. 29 (6) (2015) 377–380.

[16] D. Wilson, M.A. Langel, XPS analysis of oleylamine/oleic acid capped Fe_3O_4, nanoparticles as a function of temperature, Appl. Surf. Sci. 303 (2) (2014) 6–13.

[17] P. Mills, J.L. Sullivan, A study of the core level electrons in iron and its three oxides by means of X-ray photoelectron spectroscopy, J. Phys. D Appl. Phys. 16 (5) (2000) 723.

[18] T. Yamashita, P. Hayes, Analysis of XPS spectra of Fe^{2+}, and Fe^{3+}, ions in oxide materials, Appl. Surf. Sci. 254 (8) (2008) 2441–2449.

[19] H. Seo, M. Ogata, H. Fukuyama, Theory of the Verwey transition in Fe_3O_4, Phys. B Condens. Matter 329 (2003) 932–933.

[20] D. Schrupp, M. Sing, M. Tsunekawa, H. Fujiwara, S. Kasai, A. Sekiyama, S. Suga, T. Muro, V.A.M. Brabers, R. Claessen, High-energy photoemission on Fe_3O_4: small polaron physics and the Verwey transition, Epl 70 (6) (2005) 789–795.

[21] G.K. Rozenberg, G.R. Hearne, M.P. Pasternak, P.A. Metcalf, J.M. Honig, Nature of the Verwey transition in magnetite (Fe_3O_4) to pressures of 16 GPa, Phys. Rev. B 53 (10) (1996) 6482.

[22] R.K. Zheng, H. Gu, B. Xu, X.X. Zhang, Memory effects in a nanoparticle system: low-field magnetization and ac susceptibility measurements, Phys. Rev. B 72 (1) (2005), 014416-1.

[23] A. Lagunas, A.M.I. Payeras, C. Jimeno, V.F. Puntes, M.A. Pericàs, Low-temperature synthesis of CoO nanoparticles via chemically assisted oxidative decarbonylation, Chem. Mater. 20 (1) (2008) 92–100.

[24] S. Upadhyay, K. Parekh, B. Pandey, Influence of crystallite size on the magnetic properties of Fe_3O_4, nanoparticles, J. Alloys Compd. 678 (2016) 478–485.

[25] V. Skumryev, S. Stoyanov, Y. Zhang, G. Hadjipanayis, D. Givord, J. Nogués, Beating the superparamagnetic limit with exchange bias, Nature 423 (6942) (2003) 850.

[26] I.S. Jacobs, C. P Bean, in: G.T. Rado, H. Suhl (Eds.), Magnetism III, Academic, New York, 1963, p. 275.

[27] R.D. Mcmichael, L.J. Swartzendruber, L.H. Bennett, Langevin approach to hysteresis and Barkhausen jump modeling in steel, J. Appl. Phys. 73 (10) (1993) 5848–5850.

[28] J. Smit, H.P.J. Wijn, Ferrites, Wiley, New York, 1959, p. 158.

[29] Z.G. Zhou, Ferrite Magnetic Materials, Science Press, 1981.

[30] Y.D. Zhang, S.H. Ge, H. Zhang, S. Hui, Effect of spin disorder on magnetic properties of nanostructured Ni-ferrite, J. Appl. Phys. 95 (2004) 7130–7132.